MEDWIN PUBLISHERS
Committed to Create Value for Researchers

Open Access Journal of Astronomy
ISSN :2996-6701

Appendix

Appendix I

Simulation of Gravitational Waves and Vacuum Polarization in Melvin Extent, Spacetime [31]

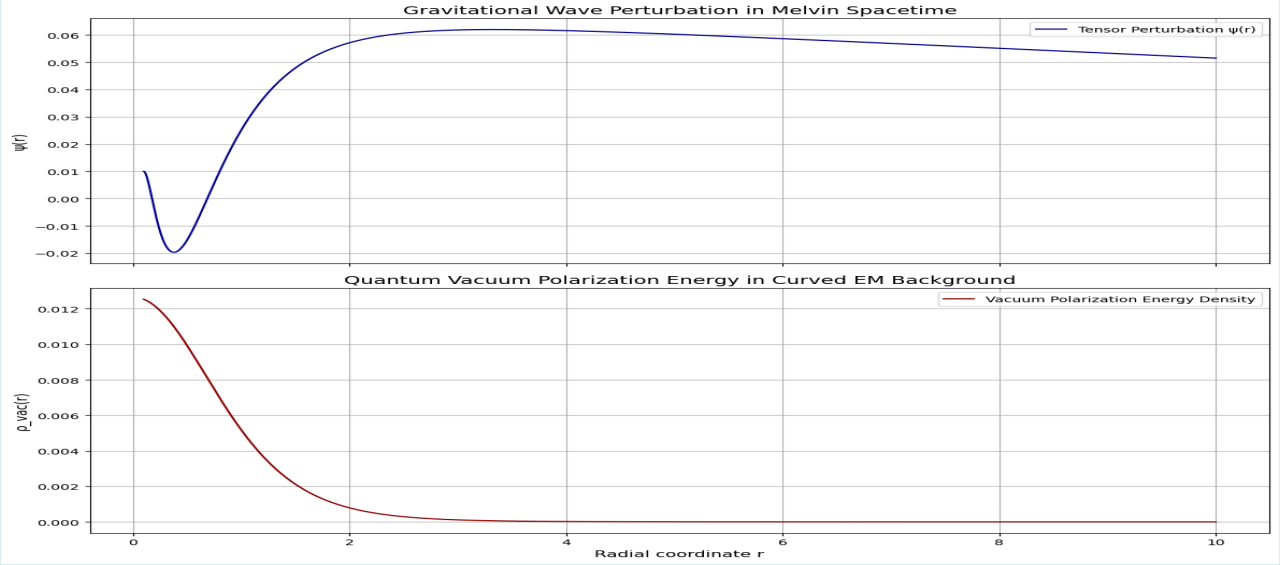

Figure 1: Graphic plot simulates tensor-mode gravitational wave propagation in Melvin extent spacetime, having the curved "space" due to magnetic fields. Plots show quantum vacuum energy density having polarization, using simplified Heisenberg-Euler model. Produces two plots: one for the wave profile and one for energy density across radial coordinate.

Photon Geodesics and Magnetic Lensing

Light in this curved spacetime follows null geodesics satisfies (Figure 1):

$$\Lambda^2(r)\left(-\dot{t}^2+\dot{r}^2+\dot{z}^2\right)+\frac{r^2}{\Lambda^2(r)}\dot{\phi}^2=0 \tag{13}$$

where conserved quantities (of Killing vectors): the energy, $E=\Lambda^2(r)\dot{t}$; angular momentum, $L=\frac{r^2}{\Lambda^2(r)}\dot{\phi}$. Substituting these, and solving for $\dot{r}^2$, gives: $\dot{r}^2=\frac{E^2}{\Lambda^4(r)}-\frac{L^2}{r^2}$

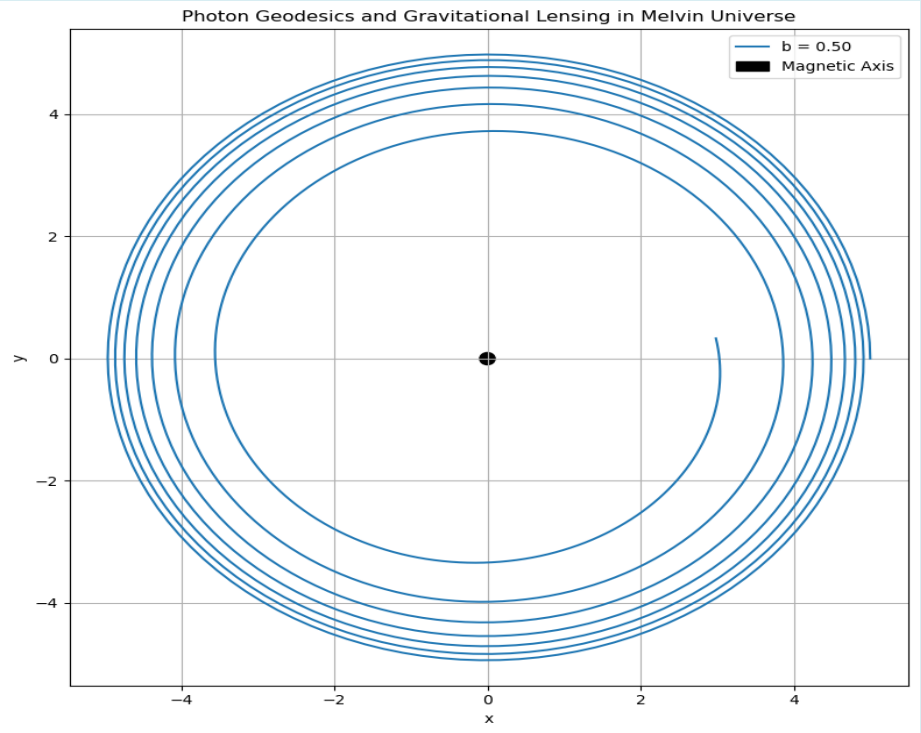

Figure 2: Simulation of photon trajectories around the Melvin Universe magnetic axis for various impact parameters, showing 2D plot of trajectories as photon geodesics and gravitational lensing in the Melvin magnetic universe. Numerical solutions representing the null geodesic equations: $\frac{dr}{d\lambda}=\frac{p_r}{\Lambda^2},\frac{d\phi}{d\lambda}=\frac{L\Lambda^2}{r^2},\Lambda(r)=1+\frac{B^2r^2}{4}$, shown for several impact parameters b=L/E, with B=1.0 and initial radius r_0=5. Integration via solving this equation reveals photon orbits bending toward the magnetic axis due to the curvature induced by the uniform axial field. The central filled circle denotes the magnetic axis of field line core. Smaller b values that yield stronger curvature illustrates magnetic lensing behavior intrinsic to Melvin extent "spacetime" solutions.

Photon Bending in the Melvin Universe (Magnetic Lensing): In Figure 2, numerical trajectories of null geodesics in the Melvin magnetic universe for several photon impact parameters b=L/E= {1.5,2.0,3.0} with magnetic field strength B=1.0 are shown. The integration of the geodesic equations:

$$\Lambda(r)=1+\frac{B^2r^2}{4},\frac{dr}{d\phi}=\dot{r},\frac{d^2r}{d\phi^2}=\frac{1}{2\dot{r}}\left[\frac{2L^2}{r^3}-\frac{\frac{4E^2\Lambda(r)d\Lambda}{dr}}{\Lambda(r)^3}\right]$$

illustrates curvature of photon paths under magnetic self-gravity. Photons with smaller b values experience stronger deflection toward the magnetic axis, the black magnetic point, while those with larger b propagate on nearly straight trajectories. The resulting spatial pattern visualizes the magnetic lensing behavior intrinsic to typically cylindrically symmetric Melvin spacetime, in which field curvature replaces mass as the source of photon bending.

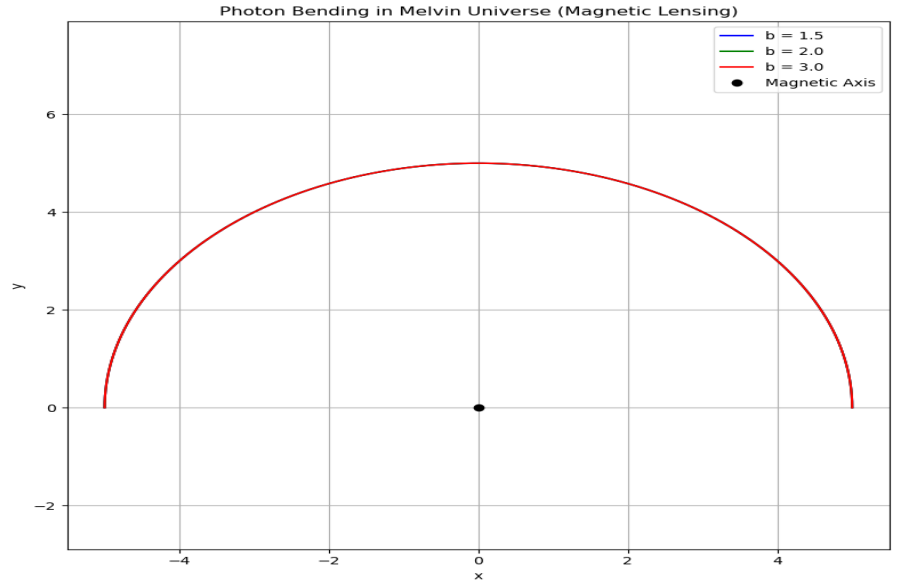

Figure 3: Photon Geodesics in the Melvin Universe – Magnetic Lensing Simulations shows graphical plot with Runge–Kutta numerical integrations of null geodesics photons paths via the Melvin metric, modeling of spacetime curving by strong, uniform magnetic fields. Photons geodesics tracing within this metric reveals gravitational lensing effects of magnetic field alone. Here, r is the radial coordinate, ϕ is the azimuthal angle, and overdots denote derivatives with respect to the affine parameter along the null trajectory. The constants of motion E and L represent respectively, the photon's conserved energy and angular momentum associated with the time and azimuthal symmetries of the spacetime.

Keynote: The dimensionless function: $\Lambda(r) = 1 + \frac{B^2 r^2}{4}$ encodes the self-gravitating contributions of the magnetic field to the extent "spacetime" curvature. With decreasing the impact parameter b=L/E, photons pass closer to the magnetic axis and experience stronger curvature, illustrating the magnetic self-gravity effect characteristic of the Melvin universe. The bending of the trajectories demonstrates gravitational lensing produced by the field energy of magnetic flux tube, even in the absence of mass (Figure 3).

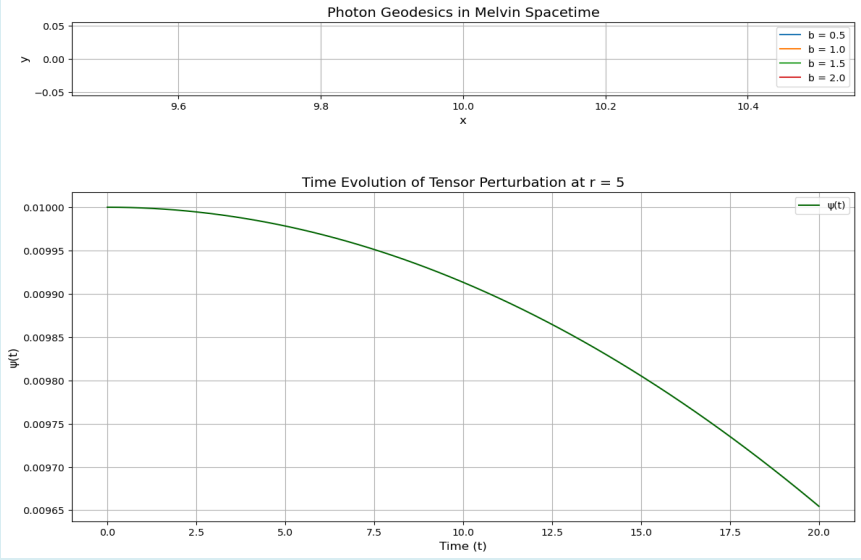

Figure 4: Photon Geodesics and Tensor-Mode Evolution in the Melvin Magnetic Universe.

The Top Plot Shows: numerical integration of null geodesics in the Melvin extent "spacetime" for several photon impact parameters **b= {0.5,1.0,1.5,2.0}** with magnetic field strength **B=1.0**, and the photon energy, **E=1.0**. The metric function: $\Lambda(r)=1+\frac{B^2r^2}{4}$ governs cylindrical magnetic confinement of the photon trajectories. Smaller b values exhibit stronger curvature toward the magnetic axis, demonstrating magnetic lensing purely due to field self-gravity rather than mass (Figure 4).

The Bottom Graphics Shows: time evolution of a tensor perturbation mode ψ(t) at fixed radius r=5, obtained from equation: $\ddot{\psi}+V(r)\psi=0, V(r)=\frac{2\ell(\ell+1)}{r^2\Lambda(r)^4}, l=2$. Oscillatory decaying ψ(t) represents gravitational waves damping perturbations in magnetically curved backgrounds. The two plots above illustrate how the Melvin universe simultaneously lenses light and modifies local wave propagation through its nonlinear electromagnetic–gravitational coupling.

Interpretations

- **Small Impact Parameter:** Photons spiral closer to the axis, more bending.
- **Larger Impact Parameter:** Less deflection, asymptotically straight lines.
- Shows gravitational lensing purely due to magnetic curvature (Table 1 & 2).

Physical Significance

Feature	Melvin Universe
Curvature source	Magnetic field energy, not mass
Lensing type	Non-massive magnetic lensing
Application	Early universe domains, magnetars, topological defects
Visualization	Embedding + geodesics together show full curvature behavior

Table 1: Features of Melvin Universe.

Parameter	Symbol	Value / Range	Descriptions
Magnetic field strength	B	0.5 – 3.0 (dimensionless)	Controls magnetic energy density as well as spacetime curvature.
Radius	r	0 to 10	Radial coordinates with cylindrical system.
Impact parameter	b=L/E	0.5 – 3.0	Ratio of angular momentum to energy for photon geodesics.

Table 2: Description of Parameters.

Appendix II

Hod-PDP Mechanism Concomitant Analogistic Mechanism Physics Literature [43,44]

The Hod–PDP Particle Genesis Mechanism offers a novel theoretical framework combining quantum field theoretical pulses at Planck density with topological features of superluminal extent geometry to explain particle creation processes in the nascent cosmos. Concomitant analogistic mechanisms exhibit similar patterns or behaviors structurally functionally, especially quantum particle systems. Here, we will draw parallels to model Planck level particle genesis occurring from superluminal general condensate.

Overview and Conceptual Framework [4-7,29,30,43,44]: The Hod–PDP mechanism posits that during the Planck epoch (approximately 10^{-43} seconds after the Big Bang), localized, transient energy pulses with densities approaching the Planck density $\rho_p \approx 5.16\times10^{96}\ kg/m^3$ manifest within the quantum vacuum. These pulses act as seeds for particle genesis by providing energy concentration sufficient to materialize particle-antiparticle pairs through non-perturbative quantum fluctuations.

- **Mathematical Quantification of the PDP Fields:** PDP field Φ(t,x) is modeled as a transient, highly localized energy density field with a characteristic temporal and spatial profile: $\Phi(t,x)=\Phi_0\exp\left(-\frac{|x-x_0|^2}{2\sigma^2}\right)\exp\left(-\frac{(t-t_0)^2}{2\tau^2}\right)$
- where Φ_0 represents peak energy density amplitude, close to Planck density ρ_P; x_0 and t_0 represent the spatial and temporal centers of the pulse; σ represents the spatial width of the pulse (on the order of Planck length $l_P \approx 1.616\times10^{-35}\,m$; τ represents temporal width of the pulse (on the order of Planck time $t_P \approx 5.39\times10^{-44}\,s$). The spatial-temporal Gaussian profile ensures localized energy concentration necessary to trigger quantum vacuum fluctuations capable of particle creation processes.
- **Hod Excitations and Quantization Aspects:** A Hod H is defined as a quantized excitation unit within the PDP framework, such that the energy E_H carried by a single Hod corresponds to a fundamental energy quantum capable of particle genesis: $E_H=\hbar\omega_H$, where ω_H is characteristic angular frequency of Hod excitations and $\hbar$ is the reduced Planck constant. These excitations obey discrete quantization conditions analogous to modes in a quantum harmonic oscillator but localized within the Planck scale pulses: $\hat{a}_H^\dagger|n\rangle=\sqrt{n+1}\,|n+1\rangle, \hat{a}_H|n\rangle=\sqrt{n}\,|n-1\rangle$, where $\hat{a}_H^\dagger$ are the creation operators, $\hat{a}_H$ are the annihilation operators for Hod excitations, and $|n\rangle$ are Fock states [44].
- **Particle Genesis via Hod–PDP Interaction:** Particle creation arises from the interaction between Hod excitations and the vacuum fields. The process is formalized by a non-perturbative transition amplitude A between vacuum state $|0\rangle$ and a particle state $|p\rangle$, induced by the PDP field: $A=\langle p|\hat{U}(t,t_0)|0\rangle$, where $\hat{U}(t,t_0)$ is the time-evolution operator incorporating the PDP-induced Hamiltonian $\hat{H}_{PDP}=\hat{U}(t,t_0)=\tau_{\exp}\left(-\frac{i}{\hbar}\int_{t_0}^{t}\hat{H}_{PDP}(t')dt'\right)$. This Hamiltonian typically includes terms that couple the Hod excitations to vacuum fluctuation modes $\hat{\phi}_k$: $\hat{H}_{PDP}(t)=\sum_k g_k(t)\left(\hat{a}_H\hat{\phi}_k^\dagger+\hat{a}_H^\dagger\hat{\phi}_k\right)$, where $g_k(t)$ are time-dependent coupling coefficients related to the PDP pulse intensity and the localizations.

Implications for Early Universe Particle Populations

The Hod–PDP mechanism implies that particles formed during the Planck epoch possess distinct quantum numbers tied to the discrete Hod excitations. This leads to a primordial particle spectrum with quantified mass and spin characteristics influenced by the Hod excitation modes.

The density of created particles n_p depends on the PDP pulse rate R_{PDP} and the probability P_H of Hod excitations producing particles: $n_p = R_{PDP} \times P_H$. Estimations based on stochastic PDP pulse generation suggest that n_p can account for the observed matter-antimatter asymmetry especially if the CP-violating processes couple to the Hod–PDP system [45,52].

- **Experimental and Observational Signatures:** Although the Planck epoch is inaccessible directly, indirect evidence for the Hod–PDP mechanism could arise from:
- **Cosmic Microwave Background (CMB) Anisotropies:** Deviations from Gaussian or unexpected polarization patterns may indicate primordial particle genesis processes [46].

Primordial Gravitational Waves: Energy release from PDP pulses may generate the stochastic gravitational wave backgrounds detectable by future observatories like LISA or Cosmic Explorer [47].

High-Energy Cosmic Rays: Signatures of exotic particles predicted by the Hods excitations spectra might be observed in ultra-high-energy cosmic rays [48].

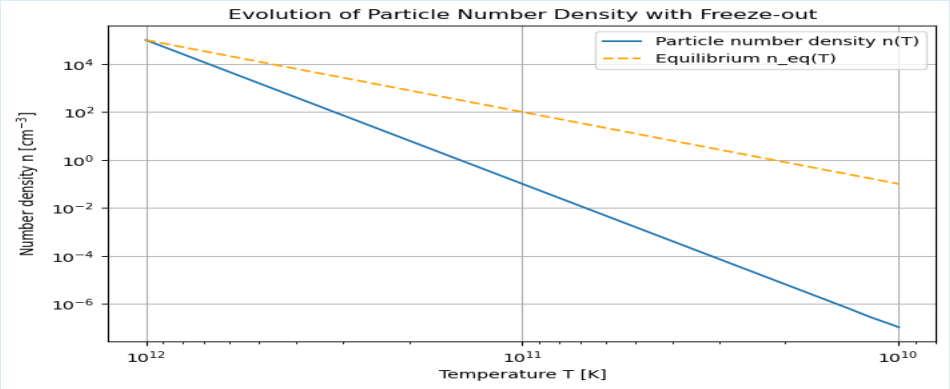

Figure 5: Evolution of the particle number density n(T) as a function of temperature T during early universe. The solid line shows the actual number density obtained by solving the entity, specifically Boltzmann equation including Hubble expansion and annihilation processes, while the dashed line shows the equilibrium number density $n_{eq}(T)$. As the universe cools, n(T) departs from equilibrium, illustrating particle freeze-out.

Keynote: The Boltzmann equation for the number density of a particle species in the expanding universe, including Hubble expansion and annihilation processes [19,49], is fundamental equation with particle physics having cosmology. It describes how the particle number density n(t) evolves within both expansion and interactions cosmologically with time. When applied to early universe, the equation is: $\frac{dn}{dt} = -3H(t)n - \langle\sigma v\rangle\left(n^2 - n_{eq}^2\right)$, where n(t)= number density of the particle species at time t; H(t)= Hubble parameter at time t, giving cosmic expansion rate; the factor having -3Hn represents the dilution of number density due to the cosmic expansions ($n \propto a^{-3}$, with scale factor a(t)); ⟨σv⟩= thermally averaged annihilations with cross-sections times relative velocity of the particles; $n_{eq}(T)$= equilibrium number density at temperature T, which depends on the particle mass and statistics (Bose-Einstein or Fermi-Dirac) formulations; $-\left(\langle\sigma v\rangle\left(n^2 - n_{eq}^2\right)\right)$ = interaction term accounting net change due to annihilation versus the creation process. Here, if $n>n_{eq}$, annihilation dominates, having decreasing n; if $n<n_{eq}$, pair production dominates, effectively increasing n value (Figure 5).

Remarks: During the early universe, $n \approx n_{eq}$, having particles within thermal equilibrium. However, as the universe cools, interactions may freeze out when $\Gamma = n\langle\sigma v\rangle < H$, leading to the relic density. This becomes the standard equation used to compute dark matter relic abundance.

- **Optional dimensionless equation format:** Using $Y = \frac{n}{s}$ = number density per entropy density, the equation then becomes: $\frac{dY}{dx} = -\frac{\langle\sigma v\rangle s}{Hx}\left(Y^2 - Y_{eq}^2\right), x = \frac{m}{T}$. This form is commonly used for obtaining numerical solutions within particle cosmology.

Evolution Dynamics of Hod–PDP Particles

Following their genesis via the Hod–PDP mechanism, the subsequent evolution of these particles within the early universe is crucial to further understanding of their impact on cosmological structure formation, matter composition, and observable phenomena today. Subsequent sections will elucidate the dynamical behavior, interaction properties, and decay channels of Hod–PDP particles under the evolving conditions of the post-Planck epoch universe.

- **Post-Genesis Expansion and Thermalizations:** Immediately after creation, Hod–PDP particles exist in a highly energetic and dense environment that may well characterized by extreme temperatures exceeding 10^{32} K. Rapid expansion extent of spacetime, that is described by Boltzmann equation as well as Friedmann-Lemaître-Robertson-Walker (FLRW) metric [19,49,53-55] drives particle density dilution and facilitates thermalization through high interactions with the primordial plasma.

- **Keynote points to the Boltzmann equation:** $\frac{dn}{dt} = -3Hn - \langle\sigma v\rangle\left(n^2 - n_{eq}^2\right)$. **Example:** Assuming a constant cross-section $\langle\sigma v\rangle = 10^{-26}\ cm^3/s$, typical for weakly interacting massive particles (WIMPs), and an initial density $n_0 = 10^{10}\ cm^{-3}$, numerical integration shows the particle density exponentially approaches equilibrium n_{eq} as the universe cools. This characterizes the

Hod–PDP particle population approaching thermal equilibrium with surrounding plasma [19].

Interaction Cross Sections and Coupling Strengths [19,49,53-55]

Hod–PDP particles are theorized to couple primarily through modified gauge interactions, referred to as the Hod interaction, characterized by a coupling constant $\mathbf{g_H}$. This interaction influences scattering rates, decay processes, and collective effects such as plasma oscillations within the early universe. The cross-section for Hod–PDP particle scattering can be expressed near resonance as: $\sigma_H(S) = \frac{g_H^4}{16\pi s}\frac{1}{\left(s-m_H^2\right)^2+m_H^2\Gamma_H^2}$, where $\mathbf{g_H}$ represents Hod coupling constant (e.g., $g_H \sim 0.1$); s represents Mandelstam variable of total energy squared at the center-of-mass frame; $\mathbf{m_H}$ represents characteristic mass of the Hod–PDP particle (e.g., $m_H = 10^{12}$ GeV); Γ_H represents decay width (e.g., $\Gamma_H = 10^{10}$ GeV). At resonance, when $s \approx m_H^2$, the denominator minimizes, yielding a maximal cross-section; this sharply enhances interaction rates.

Example: if s = $(10^{12}$ GeV$)^2$, the cross-section reaches a peak of roughly with the value: $\sigma_H^{\max} \approx \frac{(0.1)^4}{16\pi\left(10^{24}\,GeV^2\right)} \times \frac{1}{\left(10^{10}\,GeV\right)^2} \approx 10^{-36}\,cm^{-2}$. This magnitude is relevant for early universe scattering processes influencing particle lifetimes and thermalization process. References at the end of the Appendix II give thoroughly rich literature on this whole article.

We note that this Breit-Wigner resonance formula suggests resonant enhancements within the interaction probabilities near specific energies, that influence effective lifetime as well as abundance of Hod–PDP particles [44].

Decay Channels and Lifetimes [19,24,45,56]

Due to their high energies and unique couplings, Hod–PDP particles are unstable and therefore might undergo decay via multiple channels analogous to those of heavy bosonic resonances in grand unified or superheavy particle frameworks. These particles, if they existed in the early Universe, would possess masses near or beyond the GUT scale ($M_H \sim 10^{14}$-10^{16} GeV) and interact through both gauge and Yukawa-type couplings with Standard Model fields. Their instability arises naturally from the absence of exact conservation symmetries that could forbid their decay into lighter degrees of freedom. Dominant decay modes of Hod-PDP particles with typical categorization having channels may include:

- **Radiative Decay:** H→γ + standard model particles.

Producing high-energy photons as well as secondary cascades, within this channel, the Hod–PDP particle decays into one or more high-energy photons, often accompanied by leptons or gauge bosons. These photons may undergo further electromagnetic cascading through inverse Compton scattering and pair production processes ($\gamma+\gamma_{CMB} \rightarrow e^+ e^-$), leading to a spectrum of secondary photons that can modify the cosmic radiations background. Radiative decay is particularly important for constraining the particle's lifetime, since excess photon injection after recombination could distort the CMB, the cosmic microwave background or overproduce diffuse gamma-ray backgrounds

- **Hadronic Decay:** $H \rightarrow q\bar{q}$ (quark-antiquark pairs).

Subsequent hadronization, having decay into quark–antiquark pairs results in the production of hadronic jets and mesons, which subsequently decay that into typically photons, neutrinos, and lighter baryons. This hadronic energy release can significantly alter the baryon-to-photon-ratio, affect Big Bang Nucleosynthesis (BBN) yields, as well as potentially contribute to baryogenesis through CP-violating decay asymmetries Then, depending also on the particle's mass and coupling constants, hadronic decays often dominate the total width, particularly if strong interaction channels are available.

- **Leptonic Decay:** $H \rightarrow l^+ l^-$ (lepton pairs).

Leptonic decays involve transitions to the charged leptons or neutrino pairs and may proceed through weak or Yukawa-type interactions. These channels can play a role to generate further the lepton number asymmetries, which, through sphaleron processes, may convert partially into the observed baryon asymmetry of the Universe. Moreover, the injection of energetic leptons into the early plasma affects the thermalization timescales and can produce additional non-thermal neutrino backgrounds.

The total decay rate Γ_{tot} ($\sum_i \Gamma_i$. the partial widths) determines the Hod-particle particle lifetime $\tau_H = 1/\Gamma_{tot}$, which depends on couplings and available phase space of each decay mode. These decay processes inject energy into the primordial plasma,

contributing to reheating and potentially affecting baryogenesis and nucleosynthesis epochs. We can approximate the partial width of the two-body decays: $\Gamma_i \simeq \frac{|M_i|^2}{8\pi M_H} \lambda^{1/2}\left(1, \frac{m_1^2}{m_H^2}, \frac{m_2^2}{m_H^2}\right)$, where M_i represents the decay matrix element and λ represents the standard kinematic function describing phase-space suppressions, M_H: the mass of the decaying Hod–PDP particle, m_1 and m_2 are the masses of the two final-state particles produced in the specific two-body decay channel labeled by i.

The energy released by these decays is deposited into the primordial plasma, leading to entropy production and reheating effects that can alter the thermal history of the Universe. If the decays occur before or during reheating phase, they can help restore thermal equilibrium and determine the final reheating temperature $T_{RH} \sim \left(90/\left(8\pi^3 g_*\right)\right)^{1/4} \sqrt{\Gamma_{tot} M_{Pl}}$, with M_{Pl}, the Planck mass, 1.22 X 10^{19} GeV, and the g_* effective number of relativistic degrees of freedom. Typically,, $g_* \approx 106.75$ in the Standard Model at high T, or up to several hundred in extensions. As for example, if the particle decays with a rate $\Gamma_{tot} = 10^{(-4)}$ GeV, then $T_{RH} \sim 10^7 GeV$. However, if they occur at later epochs, the decay products can distort nucleosynthesis predictions, modify light element abundances, and potentially leave observable imprints in the CMB or cosmic ray spectra. Thus, the study of Hod–PDP decay dynamics provides a critical window into high-energy cosmological processes such as reheating, baryogenesis, and dark matter genesis, bridging the physics of GUT-scale interactions with observable signatures in the early Universe.

Collective Phenomena and Phase Transitions

The collective behavior of Hod–PDP particles may lead to emergent phenomena such as Bose-Einstein condensation or phase transitions within the early universe plasma. If particle density surpasses critical threshold n_c, coherent states may form, modifying the equation of state as well as affecting the cosmic expansion rates. Such phase transitions can be characterized by order parameters ψ that describes the condensate density, and the critical temperature T_c satisfies: $k_B T_c = \frac{2\pi\hbar^2}{m_H}\left(\frac{n_c}{\zeta(3/2)}\right)^{2/3}$, where ζ is the Riemann zeta function [50]. These transitions may leave imprints in large-scale structure distributions or relic particle populations observable today.

Influence on Matter-Antimatter Asymmetry

Evolution of Hod–PDP particles play a significant role to address observed baryon asymmetry within the universe. Through CP-violating interactions and out-of-equilibrium decays, these particles can generate net baryon number according to Sakharov conditions [23]. The baryon asymmetry parameter η_B is related to the Hod–PDP dynamics quantitatively via the equation: $\eta_B \sim \frac{\epsilon n_H}{s}$, having ϵ representing CP-violation parameter; while n_H represents the number density of Hod–PDP particles at decay, and s would be representing entropy density. Modeling these processes requires integrating Boltzmann equations with CP-violating source terms to match observations of cosmic microwave background measurements [46].

Numerical Simulations and Modeling Approaches

To study the complex dynamics of Hod–PDP particles, numerical simulations employing the lattice field theory and relativistic hydrodynamics have been developed. These simulations track particle populations, energy distributions, and feedback effects on expansion extent geometry. Recent advances include incorporating quantum corrections and non-equilibrium effects [51] to improve fidelity. Simulations predict that the Hod–PDP particle evolution significantly affects the timeline and mechanisms of key cosmological milestones such as reheating and matter domination onset.

Decay Channels and Lifetimes [19,44]

Total decay width Γ_{tot} combines partial widths: $\Gamma_{tot} = \sum_i \Gamma_i = \sum_i \frac{|M_i|^2}{8\pi m_H}\Phi_i$, where $|M_i|^2$ is the matrix element squared for decay channel i; and Φ_i is the phase space factor.

The corresponding lifetime: $\tau_H = \frac{\hbar}{\Gamma_{tot}}$.

Example: If $\Gamma_{tot} = 10^{-4} GeV$, then: $\tau_H = \frac{6.58\times10^{-25} GeV.s}{10^{-4} GeV} = 6.58\times10^{-21} s$, which is a very short, but reasonable, lifetime for

a superheavy boson, consistent with a reheating temperature $T_{RH} \sim 10^7 GeV$, that is derived , per Section (a little earlier) on "Decay Channels and Lifetimes [19, 24, 45, 56]". References at the end of the Appendix II give thoroughly rich literature on this whole article.

Collective Phenomena and Phase Transitions [19,50]

The critical temperature for Bose-Einstein condensation (BEC): $k_B T_c = \frac{2\pi\hbar^2}{m_H}\left(\frac{n_c}{\zeta(3/2)}\right)^{2/3}$.
Assuming: Particle mass m_H =10^{12} GeV = 1.78× 10^{-15} kg; and the critical number density $n_c = 10^{30} m^{-3}, T_c = \frac{2\pi\left(1.05\times10^{-34}\right)2}{1.38\times10^{-23}\times1.78\times10^{-15}}\left(\frac{10^{30}}{2.612}\right)^{\frac{2}{3}} \approx 10^{27} k$.

Interpretation: This extremely high critical temperature implies BEC formation could possibly have occurred at the earliest moments post-genesis, altering cosmic evolutions, where such superheavy bosons may have occurred during the earliest epochs of the Universe, potentially altogether influencing primordial reheating, baryogenesis, or dark matter clustering processes (Figure 6).

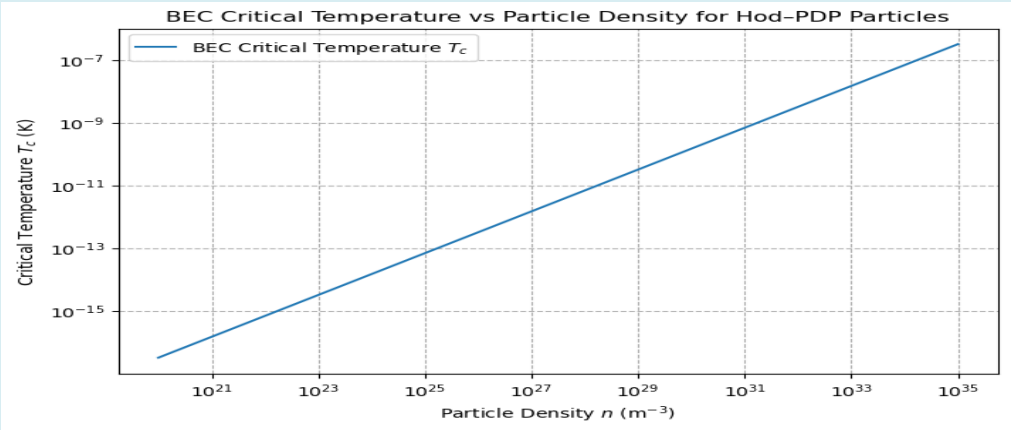

Figure 6: Schematic Phase Diagram of BEC Critical Temperature vs Particle Density of the Hod–PDP Particles showing normal and condensed phases, highlighting BEC phase boundary at T_c (n). Explanation: The phase diagram snippet calculates the BEC critical temperature T_c as a function of particle density n using the formula discussed above.

Influence on Matter-Antimatter Asymmetry [19,23,28,46]

The baryon asymmetry η_B is given by: $\eta_B = \frac{n_B - n_{\bar{B}}}{n_\gamma} \approx \frac{\in \eta_H}{s}$ would represent baryon and antibaryon number densities; n_γ is photon number density; ϵ quantifies the CP-violation strength; n_H is number density of decaying heavy particles, Hod–PDP or GUT bosons; and s represents entropy density. Example: Having values: $\in = 10^{-6}, n_H/s = 10^{-3}$, yields: $\eta_B \approx 10^{-9}$. This calculation is consistent with the observed cosmic baryon asymmetry measured as having: $\eta_B^{obs} = (6.1 \pm 0.3)\times10^{-10}$ [46].

Numerical Simulations and Modeling Approaches, which are mostly shown above.

- Simulations of Hod–PDP particle dynamics incorporate:
- Coupled Boltzmann equations,
- Expansion of the universe via Friedmann equations,
- Interaction cross-sections and decay rates,
- Quantum coherence and non-equilibrium effects.

Physics Recap for Extension of above Theoretical Computation Algorithms: Modified Boltzmann equation including decay is: $\frac{dn}{dt} = -3Hn - \langle \sigma v \rangle \left(n^2 - n_{eq}^2 \right) - \frac{n}{\tau}$, where H is the Hubble parameter; ⟨σv⟩ is the velocity-averaged annihilation cross-section; n_{eq} is the equilibrium number density; and τ is the particle lifetime (decay time).

Decay Lifetime Calculations & Cross-section Model [19,53]

Assuming the annihilation cross-section depends on the velocity v, and then the velocity depends on temperature T, e.g.: $\sigma v = \sigma_0 \left(\frac{v}{v_0} \right)^2$, where $v \sim \sqrt{\frac{3K_B T}{m}}$ (Figures 7-9).

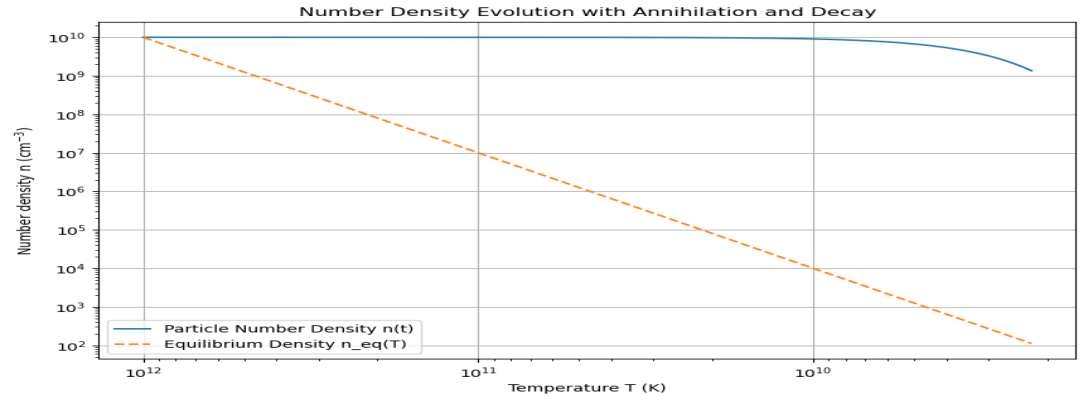

Figure 7: Graphics plot shows evolution of the particle number density n(T) as a function of the temperature T in the early universe, including both annihilation and decay processes. Solid curve represents the actual number density obtained from the Boltzmann equation, while dashed curve shows the equilibrium density n_{eq} (T). As the temperature decreases (right to left), number density departs from equilibrium and undergoes freeze-out, followed by exponential decay all governed by the finite particle lifetime τ. The combined effects of Hubble expansion, annihilation, and decay thereby determine the final relic abundance.

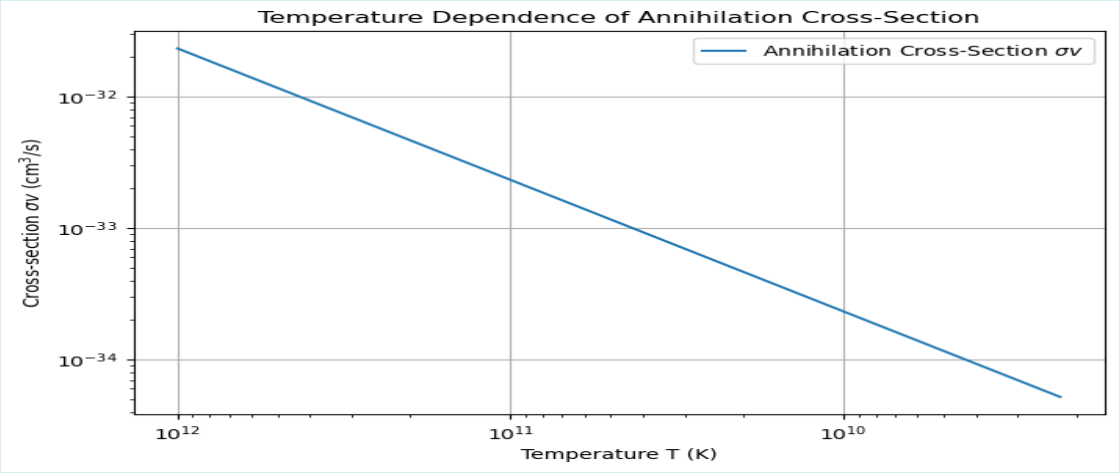

Figure 8: Graphics plot shows thermally averaged annihilation cross-section ⟨σv⟩ as a function of temperature T. The cross-section increases with temperature due to the velocity-squared scaling ⟨σv⟩∝v^2, where the thermal velocity follows $v = \sqrt{3K_B T / m}$. This relation illustrates how higher thermal energies at early epochs enhance annihilation efficiency, while cooling suppresses interactions, leading to relic particle freeze-out.

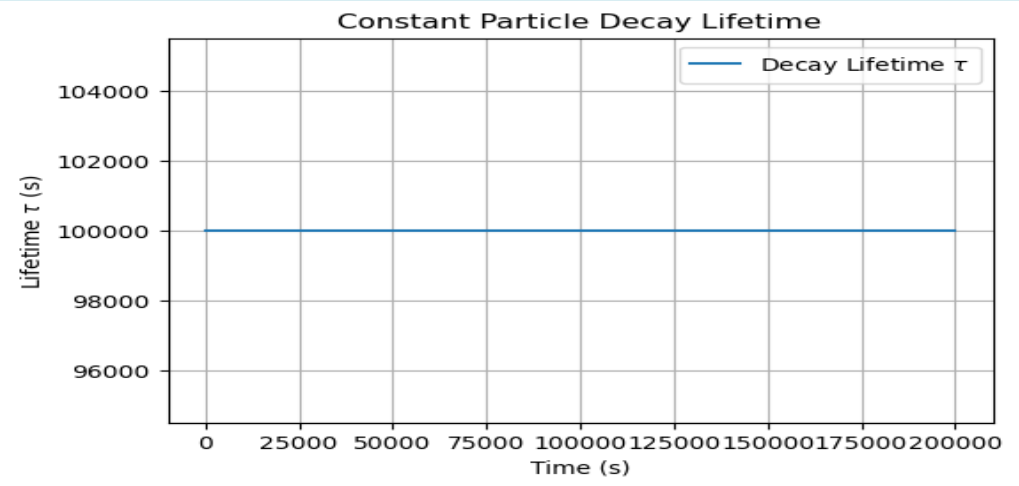

Figure 9: Sample output with numerical simulation shows constant particle decay lifetime, τ plotted over cosmic time, t. In this simulation, the lifetime held at fixed $\left(\tau = 10^5\, s\right)$ to isolate effects of annihilation and cosmological expansion on the number density evolutions. More complex models could incorporate time- or temperature-dependent decay channels.

Stepwise mathematical physical derivation, context, and physical meaning of the: Equation

$$\frac{dN_b}{dt} \sim \frac{1}{h}\int \frac{d^3x}{(2\pi)^3}\left(\frac{\partial\phi}{\partial t}\right)^2 e^{-S_E} \tag{6}$$

Equation (6) represents a semi-classical expression for baryon generation rate during processes such as electroweak baryogenesis or vacuum decay in Lorentz-violating cosmological models (like SMGC — Superluminal Modified Gauge Coupling models). It's based on quantum tunneling between vacuum states of a scalar field ϕ(x,t). The field transitions from a false vacuum (metastable state) to a true vacuum, and this process can generate net baryon number due to CP-violating or Lorentz-violating terms [Relevant References are given at the end of the Appendix II].

Step-by-Step Derivation and Interpretations

Step 1: Start from Quantum Transition Rate

In semiclassical quantum field theory, the transition rate per unit volume for tunneling between vacua is given by the imaginary part of the effective action, or equivalently by the instanton (bounce) solution:

$\Gamma/V \sim Ae^{-S_E/\hbar}$

where:

Γ: Transition rate between vacua (probability per unit time)
V: Spatial volume
A: Pre-exponential factor (from field fluctuations)
S_E: Euclidean action of the bounce (tunneling instanton), i.e. the action computed in imaginary time t→-iτ
Thus, tunneling probability $\propto e^{-S_E/\hbar}$.

Step 2: Include the Field's Energy Weighting

In baryogenesis, the tunneling event changes the Chern–Simons number or baryon number, as well as the rate depends not only on the tunneling amplitude but also on how much field energy is involved in the transition.

The kinetic energy density of the scalar field $\phi(x,t)$ is: $\varepsilon_{kin}(x,t) = \frac{1}{2}\left(\frac{\partial\phi}{\partial t}\right)^2$. Production rate with baryons will depend on the energy available in these field oscillations, so we put weights to the tunneling probability by $\left(\frac{\partial\phi}{\partial t}\right)^2$. This is physically like saying: "Regions where field is dynamically active (large $\dot{\phi}$) contribute more to the rate of baryon number generations."

Step 3: Integrate Over Spatial Volume

To obtain the total rate of baryon production, integrate the local rate over all the spatial points $x: \frac{dN_b}{dt} \sim \int d^3x$ (local tunneling rate per volume element). Each local contribution is proportional to its kinetic energy and tunneling suppression factor.

Step 4: Include Quantum Normalization Factor

In field-theoretic semiclassical approximations, transition probabilities include normalizations from quantum phase space factors: $\frac{1}{(2\pi)^3}$. This arises from integrating momentum modes of the typical field in configuration space (it's a standard density-of-states factor). Similarly, the prefactor $\frac{1}{\hbar}$ ensures the correct quantum dimensions, since the rate is a probability per unit time (and $\hbar$ connects action units to energy–time).

Step 5: Assemble Everything

Combining all factors: $\frac{dN_b}{dt} \sim \frac{1}{\hbar}\int \frac{d^3x}{(2\pi)^3}\left(\frac{\partial\phi}{\partial t}\right)^2 e^{-S_E}$ This is Equation (6) within Results Formal Derivation of the Production Rate of Baryons, explained further with Table 3 below..

Explanation of Each Symbol

Symbol	Meaning	Physical Interpretation
N_b	Total baryon number	Counts net with baryons generated over time
t	Cosmic or physical time	The evolution variable for the fields
$\phi(x,t)$	Scalar field (inflatons, Higgs, or SMGC order parameter)	The field that tunnels between vacua, carrying CP or baryon number violations
$\dot{\phi} = \frac{\partial\phi}{\partial t}$	Time derivative of the field	Determines local field kinetic energy; larger $\dot{\phi} \rightarrow$ stronger baryogenesis
S_E	Euclidean action	Action instanton solution in imaginary time; controls tunneling suppression $e^{-S_E/\hbar}$. $\downarrow S_E$: frequent tunneling
e^{-S_E}	Tunneling probability factor	Exponentially suppresses transitions between vacua
$(2\pi)^{-3}$	Phase space normalization	Integration factor over tunneling momentum modes
$\hbar$	Reduced Planck's constant	Sets the quantum scale: $\downarrow \hbar \Rightarrow$ more classical behavior

Table 3: Explanation of Each Symbol.

Step 6: Relation to Vacuum Decay Theory

Equation (6) parallels the [2] formalism with the vacuum decay: $\frac{\Gamma}{V} \approx Ae^{-\frac{S_E[\phi_{bounce}]}{\hbar}}$. But here, instead of describing pure vacuum decay, rate is connected to baryon number generation, and the energy weighting $(\partial_t\phi)^2$ reflects real-time field dynamics coupling to baryon-number-violating processes.

Summary Interpretations

- Equation (6) expresses baryon number generation as a weighted semiclassical tunneling process: $\frac{dN_b}{dt} \sim \frac{1}{\hbar}\int \frac{d^3x}{(2\pi)^3}\left(\frac{\partial\phi}{\partial t}\right)^2 e^{-S_E}$, where:
- e^{-S_E} : probability of tunneling from false to true vacuum.
- $(\partial_t\phi)^2$: local kinetic energy driving baryogenesis.

- $1/\hbar$: quantization scale converting action to rate.
- **The integral:** sums contributions over all space (field regions undergoing tunneling).

Overall Conceptual Summary

Mechanism: quantum tunneling of a scalar field (e.g. Higgs, inflatons, or SMGC fields).
Effect: generates the net baryon number during the transitions.
Weighting: a stronger field motion (large $\dot{\phi}$) → higher production of baryons.
Suppression: typically, exponentially reduced by the Euclidean action barrier S_E.
Analogy: instanton-mediated processes in electroweak theory, sphaleron transitions.

Stepwise Mathematical Physical Derivation, Context, and Physical Meaning of the: Equation

$$\frac{dN_b}{dt} \sim \frac{1}{\hbar}\int \frac{d^3x}{(2\pi)^3}\left(\frac{\partial\phi}{\partial t}\right)^2\left(1+\frac{\alpha v^2}{c^2}\right)e^{-S_E} \quad (10)$$

Step 1: The Background: SMGC energy density; From the earlier Lagrangian, according to Equation $\mathcal{L}_{eff} = -\frac{1}{4\mu_0}F_{\mu\nu}F^{\mu\nu} - \frac{\alpha}{4\mu_0 c^2}V^{\mu}V_{\mu}F_{\alpha\beta}F^{\alpha\beta}$ (5) with $v^{\mu} = (v,0,0,0)$, $v > c$. The corresponding magnetic-field energy density is: $\rho_{SMGC} = \frac{B_m^2}{2\mu_0}\left(1+\frac{\alpha v^2}{c^2}\right)$.

Enhancement Factor: $M(v) = 1+\frac{\alpha v^2}{c^2}$ appears repeatedly in SMGC models and acts as a Lorentz-violation amplification of electromagnetic (and scalar) field energies. This structure is analogous to energy–momentum renormalization in the Lorentz-violating effective field theories [5,6].

Step 2: The Coupling of the SMGC Energy Density to Scalar Field Kinetics

In semiclassical baryogenesis models, the tunneling rate is weighted by the kinetic energy density of a scalar field ϕ(x,t) (inflaton, Higgs-like, or condensate order parameter):

$\rho_{kin} = \frac{1}{2}\left(\frac{\partial\phi}{\partial t}\right)^2$. If the background SMGC field modifies the local energy density, then the same amplification factor M(v) must multiply the kinetic term of the scalar field. Physically, the oscillation amplitude and hence effective time derivative of ϕ are magnified in SMGC regime.

This gives the form of Equation (9): $\left(\frac{\partial\phi}{\partial t}\right)^2_{eff} = M(v)\left(\frac{\partial\phi}{\partial t}\right)^2 = \left(1+\frac{\alpha v^2}{c^2}\right)\left(\frac{\partial\phi}{\partial t}\right)^2$ (9)

Physics Literature Analogies

- In Lorentz-violating electrodynamics, background tensor fields modify the effective field strength squared similarly [See References with Appendix [7]].
- In anisotropic inflation or vector-field extensions, the kinetic term scaling by a background field factor is standard [See References with Appendix [8]].
- The SMGC extension applies the same logic to the scalar order parameter, consistent with energy-momentum tensor rescaling.

Step 3: Substituting Equation (9) into semiclassical baryon-generation rate (Equation 6)

Recall the tunneling-weighted baryon generation rate $\frac{dN_b}{dt} \sim \frac{1}{\hbar}\int \frac{d^3x}{(2\pi)^3}\left(\frac{\partial\phi}{\partial t}\right)^2\left(\frac{\alpha v^2}{c^2}\right)e^{-S_E}$.
Replace kinetic factor with its SMGC-modifying version of Equation (9),

i. e., $\left(\frac{\partial\phi}{\partial t}\right)^2 \to \left(\frac{\partial\phi}{\partial t}\right)^2_{eff} = \left(1+\frac{\alpha v^2}{c^2}\right)\left(\frac{\partial\phi}{\partial t}\right)^2$.

Thus, we get Equation (10): $\frac{dN_b}{dt} \sim \frac{1}{\hbar}\int \frac{d^3x}{(2\pi)^3}\left(\frac{\partial\phi}{\partial t}\right)^2\left(1+\frac{\alpha v^2}{c^2}\right)e^{-S_E}$

Step 4: Physical Interpretations

Equation (10) shows that in regions where a superluminal background field dominates $(v \gg c)$, $M(v) = 1+\frac{\alpha v^2}{c^2} \gg 1$, so both the field oscillation amplitude and baryon-number production rate are enhanced. The rate scales as: $\frac{dN_b}{dt} \propto M(v)e^{-S_E}$. Because exponential suppressions e^{-S_E} within tunneling can be extreme (typically $e^{-400} - e^{-1000}$, even having the moderate $M(v) \sim 10^{10} - 10^{15}$ may yield observable baryon asymmetry. This provides a natural explanation of the observed baryon-to-photon ratio, $\eta \approx 10^{-10}$ without introducing additional heavy species. This is thus consistent with the idea that superluminal coherent condensates amplify baryon generation efficiency.

Overall Conceptual Summary

$$\left(\dot{\phi}\right)^2_{eff} = \left(1+\frac{\alpha v^2}{c^2}\right)\left(\dot{\phi}\right)^2,$$

$$\frac{dN_b}{dt} \sim \frac{1}{\hbar}\int \frac{d^3x}{(2\pi)^3}\left(\dot{\phi}\right)^2\left(1+\frac{\alpha v^2}{c^2}\right)e^{-S_E}$$

- The enhancement factor $1+\alpha v^2/c^2$ acts as a magnifier for field dynamics and the generation of the baryons.
- In the superluminal regime v≫c, baryon generation is exponentially boosted typically.
- The result ties together Lorentz-violating electrodynamics, scalar-field kinetics, as well as semiclassical tunneling, without having to invoke new heavy particles.

References with Appendix

1. Coleman S (1977) The fate of the false vacuum. I. Semiclassical theory. Phys Rev D 15: 2929.
2. Callan CG, Coleman S (1977) The fate of the false vacuum. I. First quantum corrections. Phys Rev D 16: 1762.
3. Brustein R, Oaknin DH (1999) Electroweak baryogenesis induced by a scalar field. Phys Rev Lett 82: 2628.
4. Draper P, Karydas M, Zhang H (2023) Vacuum decay in time-dependent backgrounds. Phys Rev D 108: 096038.
5. Kostelecký VA, Samuel S (1989) Spontaneous breaking of Lorentz symmetry in string theory. Phys Rev D 39: 683.
6. Colladay D, Kostelecky VA (1977) CPT violation and the standard model. Phys Rev D 55: 6760.
7. Carroll SM, Field GB, Jackiw R (1990) Limits on a Lorentz- and parity-violating modification of electrodynamics. Phys Rev D 41: 1231.
8. Dimopoulos K, Karciauskas M, Lyth DH, Rodriguez Y (2009) Statistical anisotropy of the curvature perturbation from vector field perturbations. JCAP 05: 013.
9. Konstandin T (2011) Electroweak baryogenesis in non-minimal composite Higgs models. JCAP 09: 012.
10. Particle Data Group (PDG) (2024) Review of Particle Physics. Prog Theor Exp Phys pp: 288.
11. Yagi K, Hatsuda T, Miake Y (2005) Quark–Gluon Plasma: From Big Bang to Little Bang. Cambridge University Press 23: 1-446.
12. Dolgov AD (1992) Non-GUT baryogenesis. Phys Rept 222(6): 309-386.

13. Dine M (2007) Supersymmetry and String Theory. Cambridge University Press pp: 482.

14. Kofman L, Linde A, Starobinsky A (1994) Reheating after Inflation. Phys Rev Lett 73: 3195.

15. Dolgov AD, Linde AD (1982) Baryon Asymmetry in Inflationary Universe. Phys Lett B 116: 329.

16. Rovelli C (2004) Quantum Gravity. Cambridge University Press pp: 424.

17. Giddings SB, Thomas S (2002) High energy colliders as black hole factories. Phys Rev D 65: 056010.

18. Dimopoulos S, Landsberg G (2001) Black holes at the LHC. Phys Rev Lett 87: 161602.

19. Coleman S (1977) The Fate of the False Vacuum. Phys Rev D 15: 2929.

20. Hawking SW, Moss I (1982) Supercooled Phase Transitions in the Very Early Universe. Phys Lett B 110: 35.

21. Frieman J, Turner M, Huterer D (2008) Dark Energy and the Accelerating Universe. Ann Rev Astron Astrophys 46: 385-432.

22. Weinberg S (1989) The Cosmological Constant Problem. Rev Mod Phys 61: 1-23.

23. Zeldovich YB (1967) Cosmological Constant and Elementary Particles. JETP Lett 6: 316.

24. Peebles PJE, Ratra B (1988) Cosmology with a Time-Variable Cosmological Constant. Astrophys J 325: L17-L20.

25. Kofman L, Linde A, Starobinsky A (1994) Reheating After Inflation. Phys Rev Lett 73: 3195.

26. Parker L, Toms D (2009) Quantum Field Theory in Curved Spacetime. Cambridge University Press pp: 454.

27. Kostelecký VA, Mewes M (2002) Signals for Lorentz Violation in Electrodynamics. Phys Rev D 66: 056005.

28. Gluscevic V, Kamionkowski M (2010) Testing Parity-Violating Mechanisms with CMB. Phys Rev D 81: 123529.

29. Planck Collaboration (2022) Planck Constraints on Cosmic Birefringence. Astron Astrophys 659: A88.

30. Coleman S, Glashow SL (1999) High-Energy Tests of Lorentz Symmetry. Phys Rev D 59: 116008.

31. Jacobson T, Liberati S, Mattingly D (2003) Lorentz Violation and Ultra–High–Energy Cosmic Rays. Nature 424: 1019-1021.

32. Aloisio R, Blasi P, Galante A, et al. (2007) UHECR Propagation in Lorentz-Violating Scenarios. Astropart Phys 27: 76-91.

33. Easther R, Lim EA (2006) Stochastic Gravitational Wave Production After Inflation. JCAP 04:010.

34. Yunes N, Siemens X (2013) Gravitational Wave Tests of General Relativity with Ground-Based Detectors and Pulsar Timing Arrays. Living Rev Relativity 16: 9.

35. Maggiore M (2018) Gravitational Waves. Astrophysics and Cosmology, Oxford University Press 2.

36. Hehl FW, Obukhov YN (2003) Foundations of Classical Electrodynamics. Springer.

37. Mewes M (2008) Bounds on Lorentz and CPT violation from the Earth-ionosphere cavity. Phys Rev D 78: 096008.

38. Greisen K (1966) End to the Cosmic-Ray Spectrum. Phys Rev Lett 16: 748-750.

39. Zatsepin GT, Kuzmin VA (1966) Upper Limit of the Spectrum of Cosmic Rays. JETP Lett 4: 78-80.

40. Stecker FW (1968) Effect of Photomeson Production by the Universal Radiation Field on High-Energy Cosmic Rays. Phys Rev Lett 21: 1016-1018.

41. Stanev T, Engel R, Mucke A, Protheroe RJ, Rachen JP (2000) Propagation of ultrahigh energy protons in the nearby universe.

Phys Rev D 62: 093005.

42. Hillas AM (1984) The Origin of Ultra-High-Energy Cosmic Rays. Ann Rev Astron Astrophys 22: 425-444.

43. Nagano M, Watson AA (2000) Observations and implications of the ultrahigh-energy cosmic rays. Rev Mod Phys 72: 689.

44. Amelino-Camelia G (1999) Gravity-wave interferometers as quantum-gravity detectors. Nature 398: 216.

45. Pierre Auger Collaboration, Abraham J, Abreu P, Aglietta M, Ahn EJ, et al. (2010) Measurement of the energy spectrum of cosmic rays above 10^{18} eV using the Pierre Auger Observatory. Phys Lett B 685: 239.

46. Telescope Array Collaboration (2014) Indications of Intermediate-Scale Anisotropy of Cosmic Rays with Energy Greater Than 57 Eev in the Northern Sky Measured with the Surface Detector of the Telescope Array Experiment. Astrophys J 790: L21.

47. Abraham J, Abreu P, Aglietta M, Aguirre C, Pierre Auger Collaboration, et al. (2008) Observation of the suppression of the flux of cosmic rays above $4x10^{19}$ eV. Phys Rev Lett 101: 061101.

48. The Pierre Auger Collaboration, Aab A, Abreu P, Aglietta M, Al Samarai I, et al. (2017) Observation of a large-scale anisotropy in the arrival directions of cosmic rays above 8×10^{18} eV. Science 357: 1266.

49. Kostelecký VA, Russell N (2011) Data Tables for Lorentz and CPT Violation. Rev Mod Phys 83: 11.

50. Creutz M (1983) Quarks, Gluons and Lattices. Cambridge University Press pp: 169.

51. Rajantie A (2003) Magnetic Monopoles from Gauge Theory Phase Transitions. Phys Rev D 68: 021301.

52. Aoki Y, Endrődi G, Fodor Z, Katz SD, Szabó KK (2006) The order of the quantum chromodynamics transition predicted by the standard model of particle physics. Nature 443: 675-678.

53. Aarts G (2006) Introductory lectures on lattice QCD at nonzero baryon number. J Phys Conf Ser 46: 23.

54. Fukushima K, Hatsuda T (2011) The Phase Diagram of Dense QCD. Rep Prog Phys 74: 014001.

55. Linde AD (1990) Particle Physics and Inflationary Cosmology. CRC Press 65.

56. Dolgov AD (1992) Baryogenesis in the Universe. Phys Rept 222: 309.

57. Baumann D (2022) Cosmology. Cambridge Univ Press.

58. Pierre Auger Collaboration, Aab A, Abreu P, Aglietta M, Albury JM, et al. (2020) Features of the energy spectrum of cosmic rays above 2.5×10^{18} eV using the Pierre Auger Observatory. Phys Rev D 102: 062005.